

# Score-based diffusion models for diffuse optical tomography with uncertainty quantification

Fabian Schneider\*      Meghdoot Mozumder†  
 Konstantin Tamarov†      Leila Taghizadeh‡      Tanja Tarvainen†  
 Tapio Helin§      Duc-Lam Duong¶

February 3, 2026

## Abstract

Score-based diffusion models are a recently developed framework for posterior sampling in Bayesian inverse problems with a state-of-the-art performance for severely ill-posed problems by leveraging a powerful prior distribution learned from empirical data. Despite generating significant interest especially in the machine-learning community, a thorough study of realistic inverse problems in the presence of modelling error and utilization of physical measurement data is still outstanding. In this work, the framework of unconditional representation for the conditional score function (UCoS) is evaluated for linearized difference imaging in diffuse optical tomography (DOT). DOT uses boundary measurements of near-infrared light to estimate the spatial distribution of absorption and scattering parameters in biological tissues. The problem is highly ill-posed and thus sensitive to noise

---

\*Department of Computational Engineering, School of Engineering Science LUT University, Finland and Institute of Analysis and Scientific Computing, TU Wien, Austria (fabian.schneider@asc.tuwien.ac.at)

†Department of Technical Physics, Faculty of Science, Forestry and Technology, University of Eastern Finland, Finland (meghdoot.mozumder@uef.fi, konstantin.tamarov@uef.fi, tanja.tarvainen@uef.fi)

‡Institute of Analysis and Scientific Computing, TU Wien, Austria (leila.taghizadeh@asc.tuwien.ac.at)

§Department of Computational Engineering, School of Engineering Science, LUT University, Finland (tapio.helin@lut.fi, duc-lam.duong@lut.fi)

¶Department of Computational Engineering, School of Engineering Science, LUT University, Finland and Research Unit of Mathematical Sciences, University of Oulu, Finland (lam.duong@oulu.fi)

and modelling errors. We introduce a novel regularization approach that prevents overfitting of the score function by constructing a mixed score composed of a learned and a model-based component. Validation of this approach is done using both simulated and experimental measurement data. The experiments demonstrate that a data-driven prior distribution results in posterior samples with low variance, compared to classical model-based estimation, and centred around the ground truth, even in the context of a highly ill-posed problem and in the presence of modelling errors.

## 1 Introduction

Score-based diffusion (SBD) models provide a framework for sampling from complex distributions using empirical observations, enabling them to generate natural images from complex distributions at state-of-the-art performance [30, 15, 31]. By learning from expert-generated image data, diffusion models can capture highly complex distributions—surpassing the capabilities of classical mathematical prior models that rely on tuned parameters. In the context of Bayesian inverse problems, prior distribution modelled through diffusion models have generated significant interest due to their exceptional performance [32, 8, 12, 4, 14, 28]. They enable posterior sampling, allowing for comprehensive quantification including the posterior mean and covariance. In inverse problems these methods have been applied to challenges such as computed tomography (CT) [32, 28], magnetic resonance imaging [32], photoacoustic tomography [11] and seismic imaging [4]. The empirical data corresponding to the prior model is usually expert generated and highly realistic, but studies thus far has mostly considered simulated measurement data rather than data originating from a physical measurement. In inverse problems applications, an important challenge is evaluating methods using real measurement data, where modelling errors can degrade the performance of approaches calibrated on simplified mathematical models.

The recent developments in the use of score-based diffusion models include the introduction of regularization. More precisely, the authors of [5] introduce a Tikhonov regularized version of the score matching objective and demonstrate how it can prevent memorization, meaning that produced samples coincide with the training data.

In this work, the recent framework of unconditional representation of the conditional score function (UCoS) established in [28] is utilized. This approach is particularly well suited to large scale linear inverse problems

as it avoids repeated forward evaluations in the sampling generation by offloading the computational cost to a training process. UCoS maintains a computationally efficient, relatively low-dimensional learning problem. Additionally, UCoS circumvents the need to compute the matrix corresponding to the linear forward map. Instead, it only requires pointwise evaluations of the forward and adjoint maps, which helps mitigate memory constraints often encountered in large-scale problems.

Diffuse optical tomography (DOT) utilises boundary measurements of near-infrared light to estimate spatially distributed absorption and scattering parameters in biological tissues [1, 2, 3]. Mapping these optical parameters provide valuable information about tissue function and structure, with applications in breast cancer imaging, neonatal brain imaging, functional imaging of the adult brain, and preclinical small animal imaging [34, 16].

The image reconstruction problem in diffuse optical tomography (DOT) is a non-linear and highly ill-posed inverse problem that involves estimating the spatial distribution of optical absorption and scattering parameters [1, 2]. A linearized approximation based on a first-order Taylor expansion of the forward model (e.g., Born or Rytov approximation) is often employed [2]. In the linearized approach, changes in measured signals are considered as a linear function of the changes in the optical parameters, and is an ill-posed linear inverse problem. Given the ill-posedness of the DOT image reconstruction, regularisation techniques that assume the unknowns as smooth, sparse, or with limited changes, are typically utilized to achieve stable inversion [3]. In a similar way, Bayesian estimation incorporates prior probability distributions based on existing knowledge about the unknowns, to compute the posterior probability distribution, providing a measure of the estimates' uncertainty [18, 33]. To the best of our knowledge, diffusion models have not yet been applied to the DOT problem. This gap is addressed by studying UCoS for the DOT problem with both simulated and physical measurement data.

Recently, deep learning (DL) has emerged as a data-driven alternative to traditional model-based DOT reconstructions. One of the first attempts towards deep learned image reconstruction was carried out in [6] using a neural network comprised of fully connected and convolution layers. Yoo *et al.* [38] used convolutional framelet theory to demonstrate that a neural network can represent the DOT image reconstruction, and used a similar network architecture to estimate difference absorption coefficients. The approach was extended to use a separately trained U-Net, providing improved estimates [10]. As an alternative to these direct learned reconstructions, unrolled deep networks have also been proposed for DOT [24, 21, 37]. In this approach, an

iterative optimization algorithm is explicitly unrolled into a neural network architecture such that each iteration of the original algorithm corresponds to a layer (or block) of the network. Other approaches used co-registered ultrasound [41] or MRI [39] images to train neural networks, by incorporating a total variation-based loss between the optical parameters and the co-registered image. As it is evident, deep learning research in DOT has focused on improving its image reconstruction through advances in network architectures, integration with model-based estimation, and using complementary imaging modalities.

Nevertheless, acceptance of DL techniques in practical applications has often been restricted by opaque predictions and unreliable confidence estimates. To address this, uncertainty quantification (UQ) techniques have been proposed in deep learned imaging techniques, that can estimate confidence bounds and highlight model failures or weaknesses [19]. Traditionally, the Bayesian framework have been a natural choice for UQ, where all the unknowns and measured quantities are considered as random variables, and the uncertainty of their values are encoded into their probability distribution models. The estimated posterior distribution can be used to compute confidence intervals, and thereby quantify the uncertainty in the estimates. In practice, however, exact Bayesian inference is rarely feasible for deep networks because of its computational demands.

### 1.1 Our contribution

We study an SBD posterior sampling framework for the linearized DOT difference imaging problem based on the UCoS methodology. The framework includes a novel regularized variant that employs a convex combination of a trained data-driven score and a model-based score. In the finite-dimensional setting, we rigorously show that this convex combination locally approximates, for small diffusion times, the score associated with a geometric mixture of the corresponding probability density functions. We validate the proposed approach through extensive numerical experiments using both simulated and experimental data, covering full-view and limited-view measurement geometries as well as in- and out-of-distribution targets. The results demonstrate that incorporating a strong data-driven prior substantially reduces posterior variance in this highly ill-posed inverse problem, yielding samples that concentrate uncertainty around inclusion locations and amplitudes rather than across the full domain. We further show that the regularized UCoS variant improves robustness in limited-view and out-of-distribution scenarios, while maintaining competitive performance on ex-

perimental data. Finally, we provide a comparative assessment against the diffusion posterior sampling (DPS) method and classical model-based reconstructions, highlighting the superior fidelity and uncertainty localization achieved by UCoS-based sampling in challenging DOT settings.

## 2 Theory

Consider an inverse problem

$$y = Ax + \epsilon, \quad (1)$$

where  $y \in \mathbb{R}^m$  is the observed data,  $x \in H$  is the unknown taking values on a separable Hilbert space  $H$  and  $A : H \rightarrow \mathbb{R}^m$  is the linear forward map. We denote by  $A^* : \mathbb{R}^m \rightarrow H$  the adjoint of  $A$ . We adopt the Bayesian approach [33] to the linear inverse problem (1) and assume to have some prior knowledge of the distribution of  $x$  before any measurement is made. This knowledge is encoded in a given prior distribution  $\mu$  supported on  $H$ . The observational noise  $\epsilon \sim \mathcal{N}(0, \Gamma_{\text{obs}})$  in (1) is assumed to follow centred Gaussian distribution with covariance  $\Gamma_{\text{obs}} \in \mathbb{R}^{m \times m}$ . This approach gives rise to a posterior that is absolutely continuous with respect to the prior and its Radon–Nikodym derivative is given by,  $\mu$ -almost everywhere,

$$\begin{aligned} \frac{d\mu^y}{d\mu}(x) &= \frac{1}{Z(y)} \exp\left(-\frac{1}{2} \|Ax - y\|_{\Gamma_{\text{obs}}}^2\right), \\ Z(y) &= \int_H \exp\left(-\frac{1}{2} \|Ax - y\|_{\Gamma_{\text{obs}}}^2\right) \mu(dx). \end{aligned} \quad (2)$$

### 2.1 Bayesian ‘model-based’ estimation with a Gaussian prior

Recall that a Gaussian distribution is uniquely determined by its mean  $m$  and covariance  $S$  operator. In this section we focus on the Gaussian distribution  $\nu$  corresponding to the Ornstein–Uhlenbeck (OU) random process [7] and consider it as the prior of our Bayesian inference task. The covariance function of the OU process has the form

$$s(r_1, r_2) = \sigma^2 \exp(-\|r_1 - r_2\|/\ell) \quad (3)$$

where  $r_1, r_2 \in \Omega \subset \mathbb{R}^d$  denote the spatial locations. Here,  $\sigma$  stands for the marginal standard deviation and  $\ell$  describes the characteristic length scale of the process, i.e., the spatial distance that the parameter is expected to

have a significant spatial correlation. Moreover, we assume that the domain of interest  $\Omega$  is compact.

Since  $\Omega$  is compact, the Ornstein–Uhlenbeck covariance kernel  $s$  belongs to  $L^2(\Omega \times \Omega)$ , and the associated integral operator  $S : L^2(\Omega) \rightarrow L^2(\Omega)$  is self-adjoint, positive, and trace class. Consequently, there exists a centered Gaussian random variable taking values in  $L^2(\Omega)$  whose covariance operator is  $S$ , i.e., the Ornstein–Uhlenbeck random field admits a well-defined  $L^2(\Omega)$ -valued random variable version. Notice carefully that in this section, for convenience,  $\nu$  stands for the probability distribution of a single random function on  $\Omega \subset \mathbb{R}^d$ . However, in later sections we write  $\nu$  for the distribution of the independent product of two random functions, namely, absorption and scattering coefficients, on  $\Omega$ .

Given the Gaussian prior  $\nu$  above, the posterior  $\nu^y$  corresponding to a linear inverse problem with an additive Gaussian noise is Gaussian  $\nu^y = \mathcal{N}(\bar{x}, \Gamma_{\text{post}})$  with mean and covariance

$$\begin{aligned}\bar{x} &= m + SA^*(ASA^* + \Gamma_{\text{obs}})^{-1}(y - Am) \\ \Gamma_{\text{post}} &= S - SA^*(ASA^* + \Gamma_{\text{obs}})AS.\end{aligned}\tag{4}$$

In the discretized setting with  $H = \mathbb{R}^n$  such that  $S$  is non-degenerate, the posterior mean  $\bar{x}$  can also be seen through the lens of a Tikhonov-regularized optimization problem

$$\bar{x} = \arg \min_x [\|y - Ax\|_{\Gamma_{\text{obs}}}^2 + \|x\|_S^2]\tag{5}$$

and coincides with the *maximum a posteriori estimate*. For more details, refer to [33, 18]. In the following, we refer to this approach to the imaging task by *model-based* as it solely relies on the mathematical model for the forward map and prior distribution based on expert knowledge as opposed to being data-driven.

## 2.2 Posterior sampling using conditional score based diffusion models

For the convenience of the reader, the mathematical framework of unconditional representation for the conditional score function (UCoS), which is the main numerical contribution of this work is presented below. A more detailed introduction is found in [28].

**Conditional score–based diffusion** The mathematical setup of conditional score-based diffusion models is established in [4]. The framework

utilizes a stochastic differential equation (SDE) that transports the measure  $\mu^y$  to  $\mathcal{N}(0, \mathcal{C})$  and its reversal. This enables posterior sampling by starting from the Gaussian measure and solving the SDE backwards in time. Given  $T > 0$ , let  $\{X_t\}_{t=0}^T$  stand for the infinite-dimensional diffusion process for a continuous time process  $t \in [0, T]$  satisfying the following SDE

$$dX_t = -\frac{1}{2}X_t dt + \mathcal{C}^{1/2} dB_t, \quad (6)$$

with  $X_0 \sim \mu^y$ , where  $\mu^y$  is the posterior in (2) with prior  $\mu$ . The conditional distribution of  $X_t | X_0$  is given by

$$\mathcal{L}(X_t | X_0) = \mathcal{N}(e^{-t/2}X_0, (1 - e^{-t})\mathcal{C}),$$

where  $\mathcal{L}(\cdot)$  denotes the law of a random quantity. The process transports  $\mu^y$  to  $\mathcal{N}(0, \mathcal{C})$  as  $T \rightarrow \infty$ .

**Definition 2.1.** Define the conditional score function  $s(x, t; \mu^y)$  for  $x \in H$  as

$$s(x, t; \mu^y) = \frac{1}{1 - e^t} \left( x - e^{-\frac{t}{2}} \mathbb{E}(X_0 | Y = y, X_t = x) \right). \quad (7)$$

The following lemma follows from the arguments of [26].

**Lemma 2.2.** *Assume that  $H = \mathbb{R}^d$  and the posterior  $\mu^y$  admits a density  $q^y$ . Then the score function equals*

$$s(x, t; \mu^y) = \mathcal{C} \nabla_x \log q_t^y(x) = \mathcal{C} \nabla_x \log (q^y * k_t)(x),$$

where the convolution kernel  $k$  satisfies

$$k_t(x; z) = (2\pi(1 - e^{-t}))^{-d/2} \exp \left( -\frac{|x - e^{-t/2}z|^2}{2(1 - e^{-t})} \right). \quad (8)$$

Let the following assumption hold in this section.

**Assumption 2.3.** Let a trace class covariance operator  $\mathcal{C}$  be given. Denote by  $H_{\mathcal{C}} = \mathcal{C}^{1/2}(H)$  the Cameron-Martin space of  $\mathcal{C}$  (see [28, 9] for details) and suppose that  $\mu(H_{\mathcal{C}}) = 1$  and that for  $T > 0$

$$\sup_{t \in [0, T]} \mathbb{E} \|s(X_t, t; \mu)\|_H^2 < \infty.$$

The following theorem which is established in [4] allows us to reverse the SDE (6).

**Theorem 2.4.** *Let Assumption 2.3 hold and let  $Y_t$  solve the following SDE*

$$\begin{aligned} dY_t &= \left( -\frac{1}{2}Y_t - s(Y_t, T-t; \mu^y) \right) dt + C^{1/2} dB_t, \\ Y_0 &\sim \mathcal{L}(X_T). \end{aligned} \tag{9}$$

*Then  $\mathcal{L}(Y_T) = \mathcal{L}(X_0) (= \mu^y)$ .*

**UCoS: an efficient diffusion posterior sampling** A computationally favourable way to compute the score function (7) is the work of [28] and will be studied for the DOT problem in this work. Notice that for any discretization  $\mathbb{R}^n$  of  $H$ , the conditional score function maps  $s : \mathbb{R}^n \times \mathbb{R}^m \times \mathbb{R} \rightarrow \mathbb{R}^n$ . The approach of [28] is beneficial because the utilized score function  $r$  is lower-dimensional  $r : \mathbb{R}^n \times \mathbb{R} \rightarrow \mathbb{R}^n$  while avoiding evaluation of forward map  $A$  during sampling. This score function is given in (10) ahead.

Introduce the notations  $\lambda(t) = (e^{t/2} - e^{-t/2})^{-1}$  and

$$\begin{aligned} \Sigma_t &= (e^t - 1)\mathcal{C} - (e^t - 1)^2 \mathcal{C} A^* C_t^{-1} A \mathcal{C} \\ R_t &= (e^t - 1)I + (e^t - 1)^2 \mathcal{C} A^* C_t^{-1} \\ C_t &= (e^t - 1)A \mathcal{C} A^* + \Gamma_{\text{obs}} \in \mathbb{R}^{m \times m} \\ \xi_t(x, y) &= \mathcal{C} A^* \Gamma_{\text{obs}}^{-1} y + \lambda(t)x. \end{aligned}$$

Given these objects, define a stochastic process  $\tilde{X}$

$$\tilde{X}_t = \tilde{X}_0 + Z_t, \quad \tilde{X}_0 \sim \mu \text{ and } Z_t \sim \mathcal{N}(0, \Sigma_t)$$

with corresponding score function

$$\tilde{s}(z, t; \mu) = - \left( z - \mathbb{E}(\tilde{X}_0^\mu | \tilde{X}_t^\mu = z) \right).$$

Let the affine transformation function  $r$  of the score function  $\tilde{s}$  be given by

$$r(\eta, t; \mu) := \tilde{s}(R_t \eta, t; \mu) + R_t \eta. \tag{10}$$

The main result of [28], which will enable efficient score estimation is given in the following theorem.

**Theorem 2.5.** *Let Assumption 2.3 hold. Then the conditional score function satisfies*

$$s(x, t; \mu^y) = \lambda(t) \left( r(\xi_t(x; y), t; \mu) - e^{-t/2} x \right). \tag{11}$$

**Training in UCoS** In order to train an approximation  $r_\theta \approx r$ , define score matching (SM) loss function

$$\text{SM}_{\text{UCoS}}(r_\theta) := \mathbb{E} \left[ \lambda(t)^2 \|r(R_t^{-1}\tilde{x}_t, t; \mu) - r_\theta(R_t^{-1}\tilde{x}_t, t; \mu)\|_H^2 \right].$$

Computing the true  $r$  is in general infeasible. To address this, the denoising score matching (DSM) [35] is introduced:

$$\text{DSM}_{\text{UCoS}}(r_\theta) := \mathbb{E} \left[ \lambda(t)^2 \|r_\theta(R_t^{-1}\tilde{x}_t, t; \mu) - \tilde{x}_0\|_H^2 \right]. \quad (12)$$

By [28, Lemma 3.10],  $\text{SM}(r_\theta) = \text{DSM}(r_\theta) + V$ , where  $V$  is independent of  $\theta$ . Therefore DSM can be minimized with a known target. To efficiently sample  $R_t^{-1}\tilde{x}_t$  without computing matrices corresponding to  $A$  or their inversion, recall that by [28]

$$R_t^{-1}\tilde{x}_t = \left( \frac{1}{e^t - 1} I + \mathcal{C} A^* \Gamma_{\text{obs}}^{-1} A \right) \tilde{x}_0 + \frac{1}{\sqrt{e^t - 1}} \mathcal{C}^{1/2} z_1 + \mathcal{C} A^* \Gamma_{\text{obs}}^{-1/2} z_2 \quad (13)$$

in distribution, where  $(\tilde{x}_0, \tilde{x}_t) \sim \mathcal{L}(\tilde{X}_0, \tilde{X}_t)$  and  $z_1, z_2 \sim N(0, I)$  are independent. In section 3.2, we give an algorithmic description of training and sampling.

**Regularization based on Gaussian approximation** The authors of [5] introduce Tikhonov-regularized score matching, a regularized variant of score matching that stabilizes the score approximation by adding a quadratic norm penalty to the loss function:

$$\text{RSM}(s_\theta) := \mathbb{E} \left[ \lambda(t)^2 \left( \|s(x_t, t; \mu^y) - s_\theta(x_t, t; \mu^y)\|_H^2 + \|s_\theta(x_t, t)\|_{\Gamma_t}^2 \right) \right]. \quad (14)$$

Here,  $\|\cdot\|_{\Gamma_t}$  stands for the  $H$ -norm being weighted by a linear time-dependent operator  $\Gamma_t : H \rightarrow H$ . A non-centered version of the approach in (14) is obtained by setting

$$\text{RSM}_{NC}(s_\theta) := \mathbb{E} \left[ \lambda(t)^2 \left( \|s(x_t, t; \mu^y) - s_\theta(x_t, t; \mu^y)\|_H^2 + \|s_\theta(x_t, t) - s_0(x_t, t)\|_{\Gamma_t}^2 \right) \right], \quad (15)$$

where  $s_0$  is a known (potentially conditional) score function corresponding to another probability measure. The straightforward motivation of using a non-centered regularizer  $s_0$  is two-fold: first, centering the regularizer with a closed-form  $s_0$  such as one emerging from a Gaussian can help to encode expert information into the conditional distribution which is not necessarily

well-presented in training data. Second, the approach could be used to leverage or improve a score obtained earlier through another training data set e.g. with different resolution.

The immediate counter-argument in the context of *finite training data* is that the information encoded in  $s_0$  is not propagated to  $s_\theta$  outside the training data set. Therefore, the estimated score may miss specific expert information such as the tail behaviour. Moreover, the choice of  $\Gamma_t$  should reflect the principle that the regularization strength should diminish as the amount of training data grows.

In our quest to better enforce the expert information in scenarios with limited training data, we make the following observation. Modifying [5, Theorem 5.1], it is straightforward to show that in the infinite data limit the Tikhonov regularized score matching objective is minimized by

$$s_{\text{Tik},0}(x, t; \mu^y) = (I + \Gamma_t)^{-1} s(x, t; \mu^y) + (I + \Gamma_t)^{-1} \Gamma_t s_0(x, t),$$

where  $s$  is the (true) score function. For  $\alpha \in (0, 1)$ , the choice  $\Gamma_t \equiv \frac{\alpha}{1-\alpha} I$  yields

$$s_{\text{Tik},0}(x, t; \mu^y) = (1 - \alpha)s(x, t; \mu^y) + \alpha s_0(x, t). \quad (16)$$

Motivated by this identity, we utilize a regularized score function  $\hat{s}_{\text{Tik},\theta}(\cdot, \cdot; \mu^y, \nu^y)$  of the form

$$s_{\text{Tik},\theta}(x, t; \nu^y, \mu^y) := (1 - \alpha)s_\theta(x, t; \mu^y) + \alpha s(x, t; \nu^y), \quad (17)$$

where  $\mu^y$  is the data–driven posterior distribution of interest and  $\nu^y$  a closed-form posterior distribution, where the prior has desirable properties for the problem at hand and the corresponding score also has a closed-form. Moreover,  $s_\theta$  is the data-driven score function obtained by UCoS.

Consequently, unlike [5], we do not incorporate the regularization into the training procedure, but instead apply it directly to the trained score function during sampling. This decouples training from the choice of regularization parameter  $\alpha$ , so that different values of  $\alpha$  can be explored without repeated retraining of the score approximation.

An immediate example of a well-motivated regularizing distribution is the ‘model-based’ Gaussian posterior  $\nu^y = \mathcal{N}(\bar{x}, \Gamma_{\text{post}})$  described in Section 2.1. In the finite-dimensional setting, the score function is readily available as

$$s(x, t; \nu^y) = \mathcal{C} \left( (1 - e^{-t})\mathcal{C} + e^{-t}\Gamma_{\text{post}} \right)^{-1} (e^{-t/2}\bar{x} - x). \quad (18)$$

In fact, the setting can also be generalized to the infinite-dimensional setting, see [28, Lemma 3.8].

For convenience, we assume  $\mathcal{C} = I$  in the remainder of this section. Recall that (see Lemma 2.2) the score function of a generic distribution  $\mu$  with PDF  $p_0$  simplifies to

$$s(x, t; \mu) = \nabla_x \log(p_0 * k_t)(x),$$

where the convolution kernel  $k_t$  is given by (8). Therefore, it follows that, when  $\nu_1$  and  $\nu_2$  admit regular PDFs  $p_1, p_2$  on  $\mathbb{R}^d$ ,

$$\begin{aligned} \alpha s(x, t; \nu_1) + (1 - \alpha)s(x, t; \nu_2) &= \alpha \nabla \log(p_1 * k_t) + (1 - \alpha) \nabla \log(p_2 * k_t) \\ &= \nabla \log[(p_1 * k_t)^\alpha (p_2 * k_t)^{1-\alpha}]. \end{aligned} \quad (19)$$

It is now natural to ask whether the right-hand side of identity (19) approximates any score function in relevance to the diffusion process (6). We demonstrate by the next theorem that indeed as  $t$  decreases, the score on the right-hand side of (19) approximates locally the score of a density  $(q_\alpha / \int q_\alpha(x) dx) * k_t$ , where

$$q_\alpha(x) := p_1^\alpha(x) p_2^{1-\alpha}(x), \quad x \in \mathbb{R}^d, \quad (20)$$

is the unnormalized geometric mixture of  $p_1$  and  $p_2$ .

**Theorem 2.6.** *Assume  $p_i \in C_b^3(\mathbb{R}^d)$  such that  $Lp_i \in L^\infty(\mathbb{R}^d)$ ,  $i = 1, 2$ , and  $Lq_\alpha \in L^\infty(\mathbb{R}^d)$ , where the operator  $L$  is defined as*

$$L : C_b^3(\mathbb{R}^d) \rightarrow C(\mathbb{R}^d), \quad u \mapsto \frac{1}{2} (\Delta u + \nabla \cdot (xu)). \quad (21)$$

*Moreover, suppose  $\Omega \subset \mathbb{R}^d$  is a bounded open set and  $p_1(x), p_2(x) \geq m_\Omega$  for any  $x \in \Omega$ . Then there exists a constant  $C > 0$  and  $T > 0$  depending on  $m_\Omega$  such that for  $t < T$ ,*

$$|\nabla \log[(p_1 * k_t)^\alpha(x) (p_2 * k_t)^{1-\alpha}(x)] - \nabla \log[(q_\alpha * k_t)(x)]| \leq Ct,$$

*where the kernel  $k_t$  is defined in (8).*

*Remark 2.7.* Assume the densities  $p_i \in C_b^3$  are sub-exponential. More precisely, assume they satisfy  $p_i(x) = \exp(-r_i(x))$  for  $i = \{1, 2\}$ , where  $r_i \in C_b^3(\mathbb{R}^d)$  and

$$r_i(x) \geq -c(\|x\| + 1), \quad c \geq 0.$$

Then the assumptions of Theorem 2.6 are satisfied.

To prove Theorem 2.6, we will need the following lemma.

**Lemma 2.8.** *Let  $p$  satisfy the assumptions of Theorem 2.6. Then there exists a constant  $C > 0$  and  $T > 0$  such that for  $0 \leq t \leq T$  it holds that*

$$|\nabla \log(p * k_t) - \nabla \log p| \leq Ct. \quad (22)$$

*Proof.* We first notice that  $w(t) := p * k_t$  satisfies the Fokker-Planck-Kolmogorov equation [27, Section 5],

$$\begin{cases} \partial_t w(t) = Lw(t) \\ w(0) = p, \end{cases}$$

where the operator  $L$  is defined by (21). Thus  $L$  is the generator of the semigroup  $S(t) : C(\mathbb{R}^d) \rightarrow C(\mathbb{R}^d)$  defined as  $p \mapsto p * k_t$  for  $t \in [0, \infty)$  (see, e.g., [13, Section 7.4]). We note moreover that

$$\|S(t)p\|_\infty \leq \|p\|_\infty \int_{\mathbb{R}^d} k_t(x; z) dx = \|p\|_\infty. \quad (23)$$

Now for any  $p$  in the domain of  $L$ , thanks to the differential property of semigroups ([13, Section 7.4, Theorem 1]) and (23),

$$\|S(t)p - p\|_\infty \leq \int_0^t \|LS(s)p\|_\infty ds = \int_0^t \|S(s)Lp\|_\infty ds \leq t\|Lp\|_\infty. \quad (24)$$

By applying (24) for  $\nabla p$  we obtain

$$\|S(t)\nabla p - \nabla p\|_\infty \leq t\|L\nabla p\|_\infty. \quad (25)$$

Now since,

$$|\nabla \log(p * k_t) - \nabla \log p| \leq \frac{|\nabla(p * k_t) - \nabla p|}{p * k_t} + |\nabla p| \frac{|p * k_t - p|}{(p * k_t)p}.$$

and we observe that there exists  $T > 0$  such that on  $\Omega$  the convolution  $p * k_t$  is bounded from below by  $m_\Omega/2$ . Therefore the inequality (22) follows for some  $C > 0$  by combining (24), (25) and the fact that  $\nabla(S(t)p) = S(t)\nabla p$ .  $\square$

*Proof of Theorem 2.6.* For  $q_\alpha = p_1^\alpha p_2^{1-\alpha}$ , we have that

$$\nabla \log q_\alpha = \alpha \nabla \log p_1 + (1 - \alpha) \nabla \log p_2.$$

Therefore,

$$\begin{aligned}
& |\nabla \log [(p_1 * k_t)^\alpha (p_2 * k_t)^{1-\alpha}] - \nabla \log (q_\alpha * k_t)| \\
& \leq |\alpha \nabla \log(p_1 * k_t) + (1-\alpha) \nabla \log(p_2 * k_t) - \nabla \log q_\alpha| \\
& \quad + |\nabla \log(q_\alpha * k_t) - \nabla \log q_\alpha| \\
& \leq \alpha |\nabla \log(p_1 * k_t) - \nabla \log p_1| + (1-\alpha) |\nabla \log(p_2 * k_t) - \nabla \log p_2| \\
& \quad + |\nabla \log(q_\alpha * k_t) - \nabla \log q_\alpha|.
\end{aligned}$$

The result follows by applying Lemma 2.8 with  $p$  being  $p_1, p_2$  and  $q_\alpha$ .  $\square$

### 2.3 Unconditional score approximation

An approach for posterior sampling using score-based diffusion models is based on the unconditional score function  $s(x, t; \mu)$ , which depends only on the prior distribution and can be used to sample from the prior through a similar process as described in Section 2.2. The conditional score function, which depends on the inverse problem at hand through the measurement information is then approximated by promoting fidelity with the measurement at hand through the forward map. This method is attractive, since the unconditional score function can be paired with many inverse problems without retraining but requires significantly more computational effort in sampling since the forward map needs to be evaluated repeatedly to enforce data consistency. Since the conditioning is only approximate, fidelity with the posterior distribution is not guaranteed. DPS is established in [8] and will be used for comparison in a numerical study. The conditional score function is approximated through

$$s(x, t; \mu^y) \approx s(x, t; \mu) - \rho \nabla_x \|y - A(\mathbb{E}(X_0 | X_t = x))\|_\Gamma^2, \quad (26)$$

where  $\rho \in \mathbb{R}$  is a hyper-parameter and  $\mathbb{E}(X_0 | X_t = x)$  the expectation of the process  $X$  in (6), initiated at  $X_0 \sim \mu$ , at time  $t = 0$  conditional on its value at time  $t$ . This conditional expectation can be expressed through the score function. The gradient in (26) can in practice be implemented through auto-gradient functionality of the pytorch python package [25]. For more details for the implementation, we refer to [8].

### 2.4 Diffuse optical tomography

In a typical DOT measurement setup, near-infrared light is introduced into an object from its boundary. Let  $\Omega \subset \mathbb{R}^d$ , ( $d = 2$  or  $3$ ) denote the bounded domain with boundary  $\partial\Omega$  where  $d$  is the spatial dimension of the domain. In

a diffusive medium like soft biological tissue, the commonly used light transport model is the diffusion approximation to the radiative transfer equation [1, 2]. Here, we consider the frequency-domain version of the diffusion approximation

$$\begin{aligned} \left( -\nabla \cdot \frac{1}{d(\mu_a(r) + \mu'_s(r))} \nabla + \mu_a(r) + \frac{j\omega}{c} \right) \Phi(r) &= 0, \quad r \in \Omega \\ \Phi(r) + \frac{1}{2\zeta} \frac{1}{d(\mu_a(r) + \mu'_s(r))} \alpha \frac{\partial \Phi(r)}{\partial \hat{n}} &= \begin{cases} \frac{q}{\zeta}, & r \in s \\ 0, & r \in \partial\Omega \setminus s \end{cases}, \end{aligned} \quad (27)$$

where  $\Phi(r)$  is the photon fluence,  $\mu_a(r)$  is the absorption coefficient,  $\mu'_s(r)$  is the (reduced) scattering coefficient,  $j$  is the imaginary unit and  $c$  is the speed of light in the medium. The parameter  $q$  is the strength of the light source at location  $s \subset \partial\Omega$ , operating at angular modulation frequency  $\omega$ . Further, the parameter  $\zeta$  is a dimension-dependent constant ( $\zeta = 1/\pi$  when  $\Omega \subset \mathbb{R}^2$ ,  $\zeta = 1/2$  when  $\Omega \subset \mathbb{R}^3$ ) and  $\alpha$  is a parameter governing the Fresnel reflection at the boundary  $\partial\Omega$ , and  $\hat{n}$  is an outward unit vector normal to the boundary. The measurable data on the boundary of the object, exitance  $\Gamma(r)$ , is given by

$$\Gamma(r) = -\frac{1}{d(\mu_a(r) + \mu'_s(r))} \frac{\partial \Phi(r)}{\partial \hat{n}} = \frac{2\zeta}{\alpha} \Phi(r). \quad (28)$$

Let  $H$  be a Hilbert space that supports the infinite dimensional optical parameters  $(\mu_a, \mu'_s) \in H^2$ . By  $\mathcal{A}$  denote the forward operator that maps the optical parameters to the finite dimensional boundary data  $\Gamma \in \mathbb{R}^m$ . For frequency-domain DOT, the measured data typically consist of the logarithm of the complex boundary flux, written as

$$Y = \begin{pmatrix} \text{Re log}(\Gamma) \\ \text{Im log}(\Gamma) \end{pmatrix} = \begin{pmatrix} \text{log(Amplitude)} \\ \text{Phase} \end{pmatrix}, \quad (29)$$

so that the forward model reads

$$Y = \mathcal{A}(\mu_a, \mu'_s) + E, \quad (30)$$

where  $E$  models the additive random noise in measurements. Consider two measurements  $Y_1$  and  $Y_2$  corresponding to optical parameters  $X_1 = (\mu_{a,1}, \mu'_{s,1})$  and  $X_2 = (\mu_{a,2}, \mu'_{s,2})$ , respectively. The perturbation in the data due to changes in the parameters,  $\delta Y = Y_2 - Y_1$ , is given by the linear perturbation model [2]

$$\delta Y = J \delta X + e \quad (31)$$

where the Jacobian  $J = (\frac{\partial \mathcal{A}}{\partial \mu_a}, \frac{\partial \mathcal{A}}{\partial \mu'_s})$  denotes the Fréchet derivative of the forward operator  $\mathcal{A}$ , and  $e$  represents the measurement noise in the difference data. The linearization (31) is based on a first-order Taylor approximation and it is widely considered robust for biological targets where variations in optical properties are relatively small.

Considering a typical range of difference absorption and scattering parameters  $\delta\mu_a \in [-0.01, 0.01]\text{mm}^{-1}$  and  $\delta\mu'_s \in [-1, 1]\text{mm}^{-1}$  [17], we define the following affine transforms

$$\tilde{\delta\mu}_a(r) = \frac{\delta\mu_a(r) + 0.01}{0.02}, \quad \tilde{\delta\mu}'_s(r) = \frac{\delta\mu'_s(r) + 1}{2}, \quad r \in \Omega$$

where the rescaled optical parameters  $x = (\tilde{\delta\mu}_a, \tilde{\delta\mu}'_s)$  lie in the range  $[0, 1]$ . The linear model is obtained by substituting these into the model (31)

$$y = Ax + \epsilon, \quad (32)$$

where  $A = (0.02 \frac{\partial \mathcal{A}}{\partial \mu_a}, 2 \frac{\partial \mathcal{A}}{\partial \mu'_s})$  is the scaled Jacobian,  $x \in H, y \in \mathbb{R}^m$  and the noise term  $\epsilon \in \mathbb{R}^m$  is given by an affine transformation of the measurement noise  $e$  in (31).

### 3 Simulations

#### 3.1 Data generation

In the numerical studies, the domain  $\Omega \subset \mathbb{R}^2$  was a circle. We considered three simulation setups as shown in Fig. 1, and listed below:

- **Full-view setup:** A circular domain of radius 25 mm, with 20 sources and 20 detectors modelled as 1 mm wide surface patches located at equi-spaced angular intervals on the boundary.
- **Limited-view setup:** A circular domain of radius 25 mm, with 10 sources and 10 detectors modelled as 1 mm wide surface patches placed at equally spaced angular intervals over a 180° boundary segment.
- **Simulated experimental setup:** A circular domain of radius 40 mm, with 16 sources and 16 detectors, modelled as 8 mm and 0.6 mm wide surface patches respectively, at equally spaced angular intervals on the boundary. This simulation geometry mimics a 2D slide of the experimental setup, described later in Section 4.

For the full-view and limited-view configurations, the background optical parameters were set to  $\mu_a = 0.01 \text{ mm}^{-1}$  and  $\mu'_s = 1 \text{ mm}^{-1}$ , with an angular

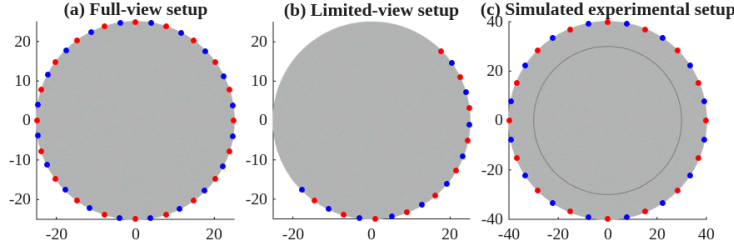


Figure 1: 2D simulation domains. Locations of the sources and detectors are shown as red and blue dots (·) on the domain boundaries. Axes units are in millimetres.

modulation frequency of  $\omega = 100$  MHz. In the simulated experimental setup, corresponding to the time-domain DOT system (described later in Section 4), the background optical parameters were  $\mu_a = 0.0065$  mm $^{-1}$  and  $\mu'_s = 0.95$  mm $^{-1}$  within a 30 mm radius, and  $\mu_a = 0.01$  mm $^{-1}$  and  $\mu'_s = 0.8$  mm $^{-1}$  in the outer region. The modulation frequency was  $\omega = 56.98$  MHz, corresponding to the Fourier-transformed time-domain measurements obtained from the experimental system.

The linear operators  $A$  were computed for each setup using a finite element (FE) approximation of the solution to Eq. (32). The FE approximation employed the standard Galerkin method, as implemented using the Toast++ software [29]. While solving the forward problem to generate the measurements, the operator  $A$  was computed on a 2D mesh with 12853 nodes and 25326 triangular elements. For the inverse problem,  $A$  was instead computed on a mesh with 11329 nodes and 22302 triangular elements to avoid an inverse crime. The unknown parameters were represented as 32×32 pixel images. The random measurement noise  $\epsilon$ , in Eq. (1), was assumed to be an additive zero-mean Gaussian distribution  $\mathcal{N}(0, \Gamma_{\text{obs}})$ . Assume further that  $\Gamma_{\text{obs}}$  is diagonal with standard deviation  $\sigma = 0.05$  for logarithm of amplitude and  $\sigma = 0.001$  for phase; this corresponded to roughly 1% of the mean data values. While solving the inverse problem, the noise mean and covariance were assumed to be known.

### 3.2 Training and evaluation

**Training** Training dataset  $(x_i)_{i=1}^N$  is given by  $N = 10,000$  images with 2 independent channels corresponding to absorption and scattering coefficients. Each channel has a random number of one to three circular inclusions.

sions with random position and value. The inclusion radii were drawn from a uniform distribution  $U_{(0,10)}$  mm, and their contrast were sampled from a uniform distribution  $U_{(0,1)}$ . Taking equations (12) and (13) into account, training can be performed using algorithm 1.

---

**Algorithm 1** Training a score approximation  $r_\theta$

---

- 1: **Input:** Neural network  $r_\theta$ , training data  $\mu = \frac{1}{N} \sum_{i=1}^N \delta_{x_i}$
- 2: **Output:** Trained score function  $r_\theta$
- 3: **while** Training **do**
- 4:     Sample  $\tilde{x}_0 \sim \mu, t \sim U_{[\varepsilon, 1]}$       $\triangleright U_{[\varepsilon, 1]}$  is uniform distribution on  $[\varepsilon, 1]$
- 5:     Sample  $z_1, z_2 \sim \mathcal{N}(0, I)$
- 6:      $R_t^{-1} \tilde{x}_t \leftarrow \left( \frac{1}{e^{t-1}} I + \mathcal{C} A^* \Gamma_{\text{obs}}^{-1} A \right) \tilde{x}_0 + \frac{1}{\sqrt{e^{t-1}}} \mathcal{C}^{1/2} z_1 + \mathcal{C} A^* \Gamma_{\text{obs}}^{-1/2} z_2$
- 7:     Perform minimization step on  $\|r_\theta(R_t^{-1} \tilde{x}_t, t; \mu) - \tilde{x}_0\|^2$ .
- 8: **end while**

---

The model is trained for 20 epochs using the AdamW [22] optimizer, a modification of the Adam optimizer, which integrates weight decay to the gradient. Learning rate is chosen in range from 0.002 to 0.0005, decaying linearly through the epochs. The truncation hyper-parameter  $\varepsilon$  in algorithm 1 is set to  $\varepsilon = 0.001$ . The Operator  $r_\theta$  is parametrized as a Fourier-Neural Operator [20]. The architecture is based on [4] and uses -first- a fully connected lifting layer that maps the input with channels corresponding to unknown  $x$ , time  $t$  (and for conditional approach measurement  $y$ ) to a 32 dimensional lifted space, -second- 10 Fourier neural layers with 32 nodes and 17 Fourier modes and -finally- two fully connected layers with non-linear activations that map back to the original resolution. On a Nvidia A100 GPU with capacity of 80 GiB of memory, one epoch takes approximately 40 seconds. The actual memory usage during training is < 5 GiB. Furthermore, similar to [4, 28], a time change  $\beta(t) = 0.05 + t(10 - 0.05)$  in the forward and backward SDE is employed.

**Sampling** To sample from the posterior distribution, the reverse SDE (9) under utilization of Eq. (11) is discretized in time though a reverse time Euler-Maruyama method, see [32, 27] for details. Algorithm 2 gives more details on the precise sampling approach including the use of Euler-Maruyama method. For sampling, set  $\varepsilon = 0.005$ ,  $T = 1$  and use  $k = 500$  time-steps in the reverse SDE. On a Nvidia A100 GPU, generating 100 samples without and with regularization in parallel takes approximately 5 and 8 seconds, respectively. For numerical experiments, the parameters

---

**Algorithm 2** UCoS posterior sampling

---

- 1: **Input:** Score approximation  $r_\theta$ , measurement data  $y$ , time steps  $T = t_k > t_{k-1} > \dots > t_1 > t_0 = \varepsilon$ , Gaussian unconditional score function  $s(x, t; \nu)$
- 2: **Output:** Posterior sample  $x \sim \mu^y$
- 3:  $\gamma \leftarrow \mathcal{C} A^* \Gamma_{\text{obs}}^{-1} y$
- 4:  $x_T \sim \mathcal{N}(0, \mathcal{C})$
- 5: Precompute  $\bar{x}, \Gamma_{\text{post}}$  given by (4)
- 6:  $\Delta t \leftarrow T/n$ ,
- 7: **for**  $i = n, \dots, 0$  **do**
- 8:    $z_i \sim \mathcal{N}(0, I)$
- 9:    $\xi_i = \gamma + \lambda(t_i) x_{i+1}$
- 10:    $s(x_i, t_i; \mu^y) \leftarrow \lambda(t_i) (r_\theta(\xi_i, t_i; \mu) - e^{-t_i/2} x_{i+1})$
- 11:    $s(x_i, t_i; \nu^y) \leftarrow \mathcal{C} ((1 - e^{-t_i}) \mathcal{C} + e^{-t_i} \Gamma_{\text{post}})^{-1} (e^{-t_i/2} \bar{x} - x_{i+1})$
- 12:    $s_i \leftarrow (1 - \alpha) s(x_i, t_i; \mu^y) + \alpha s(x_i, t_i; \nu^y)$
- 13:    $x_i = (-x_{i+1}/2 - s_i) \Delta t + \mathcal{C}^{1/2} (\sqrt{\Delta t}) z_i$
- 14: **end for**

---

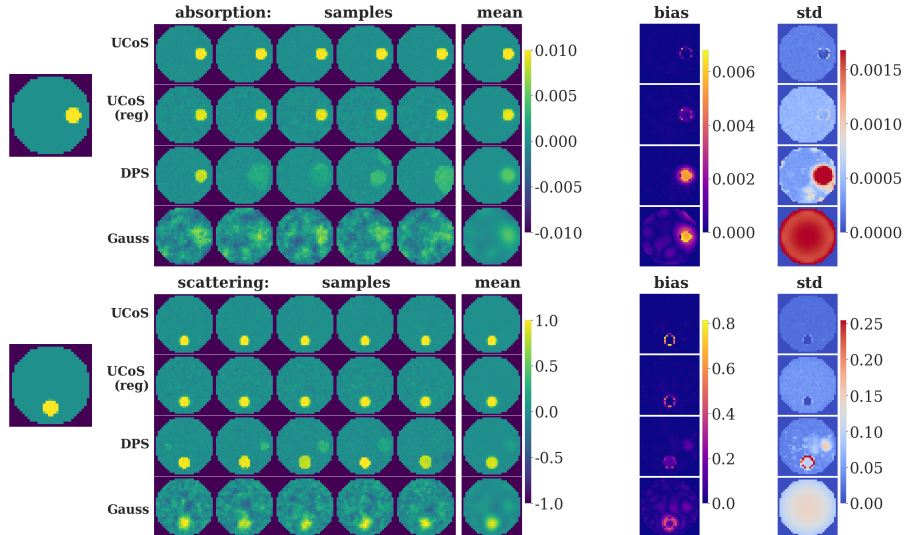
$\alpha = 0.5$  is used in the regularized approach for simulated data, and  $\alpha = 0.4$  for the experimental data.

### 3.3 Results

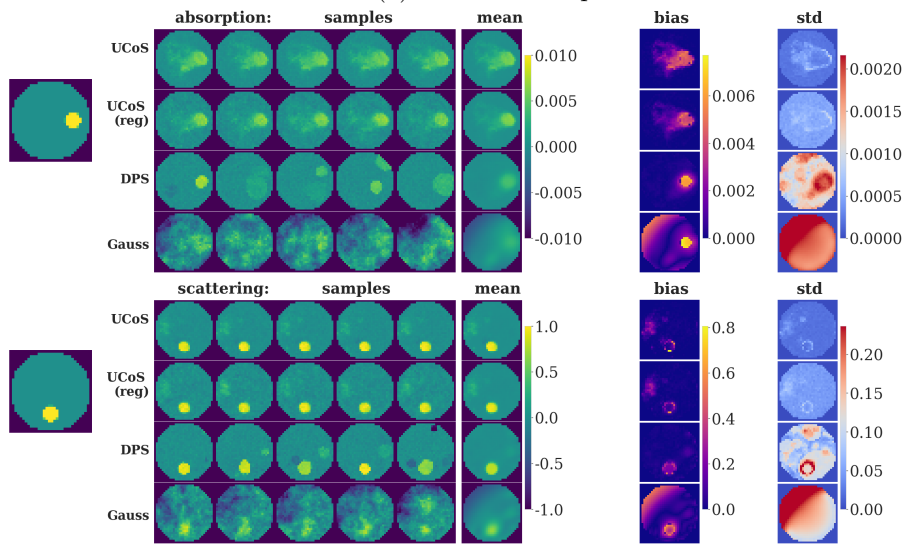
In this section, we generate posterior samples based on simulated measurements and compare the performance of UCoS, regularized UCoS, DPS [8], and a posterior derived from a Gaussian Ornstein–Uhlenbeck process prior as outlined in Section 2.1. The targets used for these experiments are a single inclusion in Figure 2 and two inclusions in Figure 3. Figure 4 presents a summary of the posterior samples for an out-of-distribution target. Figures 2 (a), 3 (a) and 4 (a) correspond to results from simulated data for the full view setup and Figures 2 (b), 3 (b) and 4 (b) to limited view setup.

Let us first inspect the samples supported by the prior in Figures 2 and 3. UCoS generates posterior samples that are highly consistent with the ground truth, exhibiting low variance primarily localized around the inclusions. In particular, for the limited view setup, the regularized approach produces relatively sharp, circular inclusions. In contrast, DPS generates samples with means that are close to the truth but exhibit much larger variation in both the number and position of the inclusions. The variance in DPS is spread over a much larger area than in UCoS. The Gaussian pos-

terior samples show substantial variance across the entire domain. While the mean is somewhat consistent with the ground truth, the individual samples are heavily corrupted by this large variance. Notably, in the limited view case, the individual samples fail to capture circular inclusions. In the out-of-distribution case (Figure 4), UCoS samples capture the elliptical and triangular shapes well. The method achieves this by placing a large circular inclusion for absorption and two smaller ones for scattering. Regularized UCoS slightly merges the two small circles into one connected shape. In the limited view setup, UCoS struggles to capture the smaller triangular inclusion for absorption. However, regularized UCoS places a small circular inclusion at the location of this inclusion in the mean sample. For scattering, regularized UCoS places a large circle at the location of the elliptical scattering shape. In DPS, the mean generally aligns well with the ground truth but shows a larger variance, especially in terms of shape and the number of inclusions. The ellipse for the absorption coefficient is captured most accurately by DPS in the full view setup. However, the triangular inclusion for absorption is less visible in DPS. Many samples show no inclusion at that location in both the full and limited view setups. The samples based on the Gaussian OU process prior perform similarly to the previous two cases. There is significant variance across the samples, which is spread across the entire domain. While the inclusions are somewhat visible in the averages, individual samples remain quite noisy.

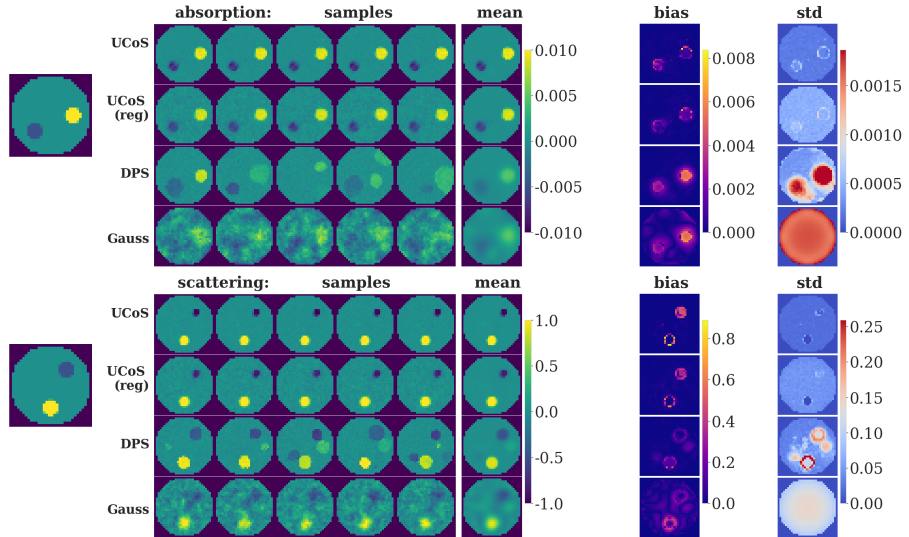


(a) Full view setup

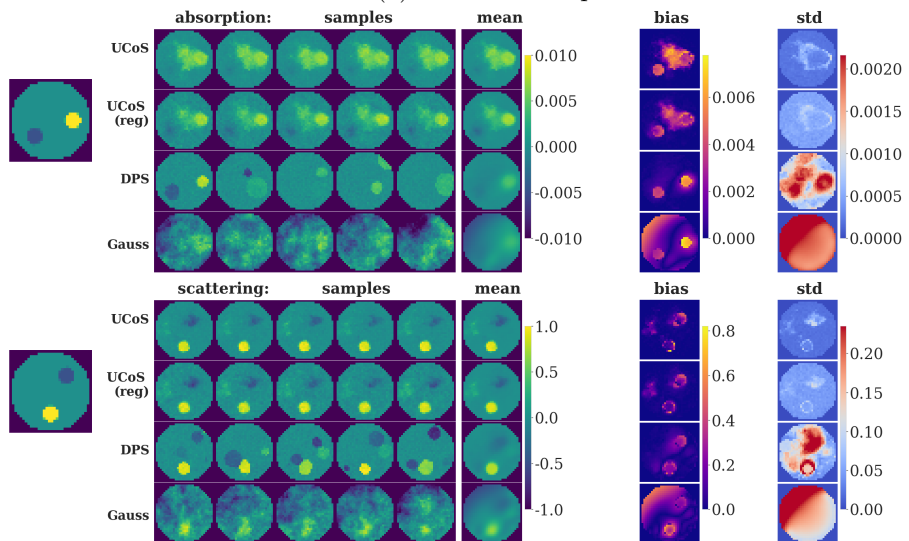


(b) Limited view setup

Figure 2: Simulated DOT with one target inclusion with (a) the full view and (b) the limited view setup. Columns from left to right: simulated ground truth (first column), five posterior samples (columns 2-6), an average (column 7), bias (column 8) and standard deviation (column 9), which are computed over 100 generated samples. The methods used from top to bottom: UCoS, regularized UCoS, DPS, Gaussian OU process prior.



(a) Full view setup



(b) Limited view setup

Figure 3: Simulated DOT for two target inclusions with (a) the full view and (b) the limited view setup. Columns from left to right: simulated ground truth (first column), five posterior samples (columns 2-6), an average (column 7), bias (column 8) and standard deviation (column 9), which are computed over 100 generated samples. The methods used from top to bottom: UCoS, regularized UCoS, DPS, Gaussian OU process prior.

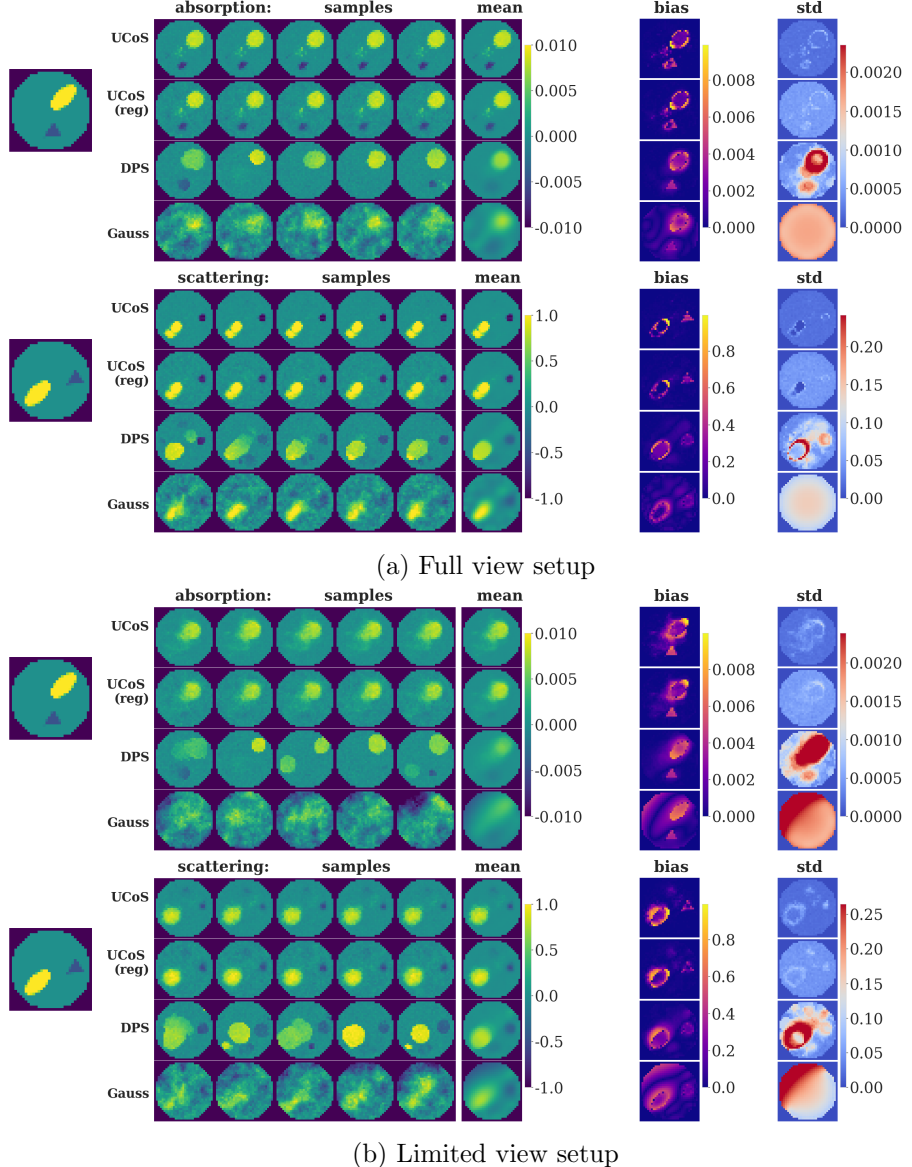


Figure 4: Simulated DOT with two out-of-distribution inclusions with (a) the full view and (b) the limited view setup. Columns from left to right: simulated ground truth (first column), five posterior samples (columns 2-6), an average (column 7), bias (column 8) and standard deviation (column 9), which are computed over 100 generated samples. The methods used from top to bottom: UCoS, regularized UCoS, DPS, Gaussian OU process prior.

## 4 Experimental

### 4.1 Measurement setup

The measurements were performed using the time-domain DOT setup in the University of Eastern Finland [23]. In the experiments, light pulses with an approximate duration of  $200 \sim 3$  ns were generated for each source-detector channel pair (repetition rate of 10 Hz, pulse energy 0.12 mJ, wavelength 808 nm) were generated via a Nd:YAG laser with optical parametric oscillator (NT352B, Ekspla Uab), guided to a phantom via fiber optics and collected via an avalanche photodiode (APD430A, Thorlabs). The laser pulse-to-pulse variation was measured with the second Si biased photodetector (DET025AFC, Thorlabs). The signals from both photodetectors were digitized by high-bandwidth oscilloscope (WavePro 254HD, Teledyne LeCroy) with 12-bit dynamic range and sampling period of 50 ps. The digitized signals were then converted to frequency-domain and used for image reconstruction. The source and detectors were located at  $z = -5$  mm and  $z = 5$  mm from the vertical centre of the phantom at  $z = 0$  mm.

The cylindrical phantom consisted of an outer solid and inner liquid parts (Fig. 5). The solid part was made of epoxy resin combined with  $\text{TiO}_2$  powder and toner[40] providing absorption  $\mu_a = 0.01 \text{ mm}^{-1}$  and reduced scattering  $\mu'_s = 0.8 \text{ mm}^{-1}$  coefficients at 800 nm. The solid part had inner and outer diameters of 60 mm and 80 mm, respectively. The liquid part consisted of 1% SMOFlipid (Fresenius Kabi) and 0.001% India ink which gave approximately  $\mu_a = 0.0065 \text{ mm}^{-1}$  and  $\mu'_s = 0.95 \text{ mm}^{-1}$ . Inclusions were made by filling polypropylene tubes (diameter 6 mm, wall thickness 0.5 mm) with different concentrations of Indian ink, intralipid or contrast agents such as indocyanine green (ICG) or light absorbing black porous silicon nanoparticles (Si NPs)[36].

Training and evaluation of UCoS for the experimental data was carried out similarly as described earlier in Section 3.2. For training, simulated data was used, as described earlier in Section 3.1. During sampling, the measured and Fourier transformed data from the different targets were used as the  $y$  data.

### 4.2 Results

In this section, the results of the measurement experiments are summarized in Figures 6 and 7 for different unknown targets. While we do not have access to the exact absorption and scattering coefficients of the phantoms,

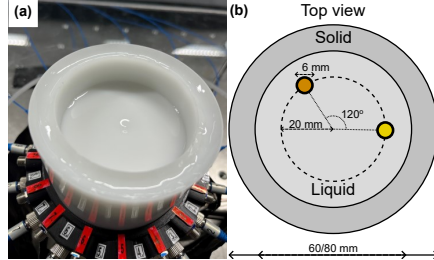


Figure 5: (a) Photograph of the cylindrical phantom used in DOT experiments. (b) Top view of the phantom with inclusions.

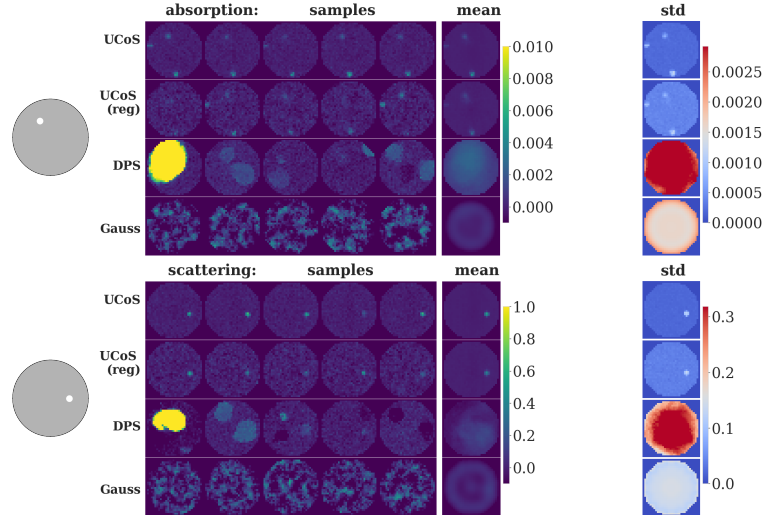
we can estimate their values with reasonable accuracy and we do know the exact positions of the inclusions.

Overall, both UCoS and regularized UCoS generate samples that closely align with the positions of the phantoms, showing very little difference between the two methods. These samples typically place inclusions at what we believe to be the correct locations (see Figures 6(a, b) and the absorption results in Figure 7(a, b)). Moreover, there is minimal variance in terms of both position and amplitude. The variance is mostly concentrated around the true locations of the inclusions, with negligible variance away from these points.

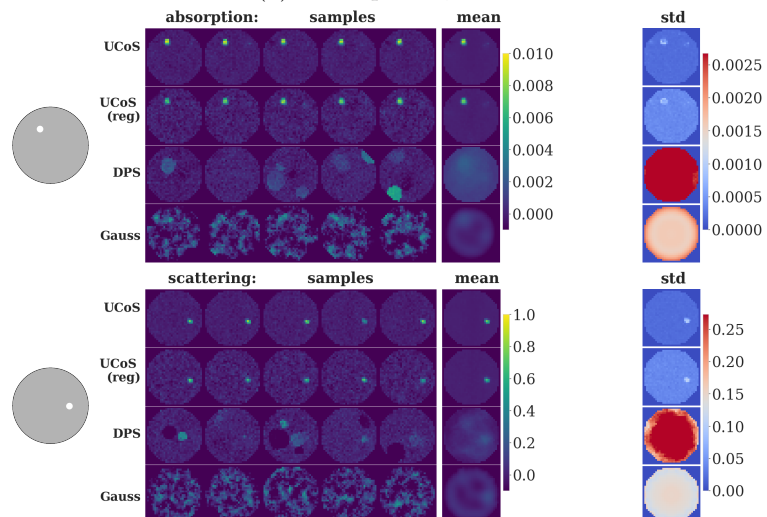
In contrast, DPS generates samples with significant variation in both size and location, and occasionally produces artifacts that deviate from the prior (for example, the first sample in Figure 6(a) shows inconsistencies in absorption and scattering). The variance in DPS is not confined to the regions of the true inclusions but extends across the entire domain. While the mean of the samples can sometimes align with the truth (e.g., Figure 6(b) and absorption coefficients in Figure 7), the overall quality is less consistent.

For the Gaussian posterior samples, we observe a large posterior variance across the entire domain. The individual samples do not exhibit well-defined circular inclusions and appear much rougher in comparison. Similar to DPS, the mean posterior occasionally matches the true values (e.g., Figure 6(b) and absorption coefficients in Figure 7).

In some instances, all methods struggle to accurately estimate the scattering coefficient, as seen in Figure 7.



(a) Intralipid x2, ink x2



(b) Intralipid x5, ink x5

Figure 6: Reconstructions using the experimental data measured in phantoms with two inclusions containing: (a) two times increased concentration of ink (absorption inclusion) or intralipid (scattering inclusion) as compared to the background phantom; (b) same as (a) but with five times increased concentrations. Rows in each panel show different reconstruction methods listed from top to bottom: UCoS, regularized UCoS, DPS, Gaussian OU process prior. Each row presents from left to right: approximate ground truth, 5 samples, sample average and standard deviation.

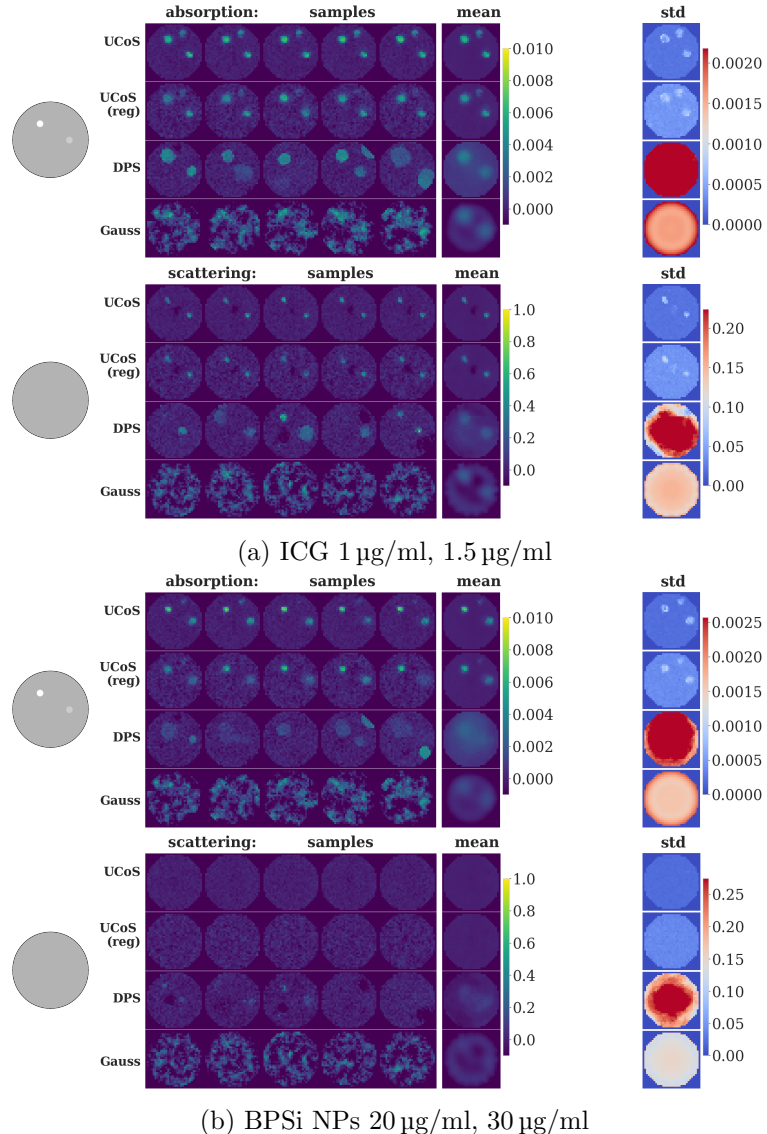


Figure 7: Reconstructions using the experimental data measured in phantoms with two inclusions containing: (a) ICG 1  $\mu\text{g/ml}$  and 1.5  $\mu\text{g/ml}$ ; (b) BPSi NPs 20  $\mu\text{g/ml}$  and 30  $\mu\text{g/ml}$ . Rows in each panel show different reconstruction methods listed from top to bottom: UCoS, regularized UCoS, DPS, Gaussian OU process prior. Each row presents from left to right: approximate ground truth, 5 samples, sample average and standard deviation.

## 5 Discussion and Conclusions

The SBD method UCoS for posterior sampling in the linearized DOT difference imaging problem was presented including a novel regularized approach to UCoS that introduces the convex combination of two score functions. In the finite dimensional case, the behaviour of the convex combination was studied in terms of the score of the geometric mixture of the probability density functions (PDFs) for small time values.

The methodology was evaluated with numerical simulations for a full-view and limited-view setup and experiments for a full-view setup. The results show that a strong data-driven prior distribution can help reduce the variance of posterior samples in the highly ill-posed problem. More precisely, the discussed method generates samples that are highly consistent with ground truth values, exhibiting relatively low variance. Unlike traditional model-based approaches, where variance tends to spread across the entire domain (Figs. 2–4, Gauss rows), the variance here is mainly confined to the location and amplitude of the inclusions. This makes the method particularly advantageous in producing results that closely resemble the true underlying data.

The method performs well in both full and limited-view setups, and shows robust performance when tested with both in-distribution and out-of-distribution ground truth values (Figs. 2–4). Notably, the regularized version of this method outperforms the plain UCoS in limited-view or out-of-distribution scenarios, offering a slight improvement in these cases.

Crucially, even in the presence of real-world data that violate common assumptions about the forward map and observational noise, UCoS methods consistently yield convincing reconstructions, surpassing the performance of classical model-based techniques as well as other approximate SBD approaches. Still, reconstruction with experimental data remains challenging for UCoS, as it occasionally misses inclusions or generates "hallucinated" inclusions that do not reflect reality. This issue is not unique to UCoS; similar artefacts are seen in classical model-based reconstructions. In fact, across the experiments, UCoS consistently produces the most desirable posterior samples with low variance around the inclusions and high fidelity to the ground truth. No significant change in performance was observed with regularization when applied to experimental data.

In contrast, the SBD method DPS produces samples with high variance, not only in the location and amplitude of inclusions, but also in the number of inclusions. This high variance means that the average of these samples often contains little useful signal. While model-based reconstructions tend

to capture inclusions slightly less accurately than UCoS on average, the individual samples are heavily corrupted by noise, making it hard to extract any meaningful signal from them.

## References

- [1] Simon R Arridge. “Optical tomography in medical imaging”. In: *Inverse Problems* 15.2 (1999), R41.
- [2] Simon R Arridge and John C Schotland. “Optical tomography: forward and inverse problems”. In: *Inverse problems* 25.12 (2009), p. 123010.
- [3] Andrea Aspri et al. *Mathematical and numerical challenges in diffuse optical tomography inverse problems*. 2024. DOI: 10.3934/dcdss.2023210.
- [4] Lorenzo Baldassari et al. “Conditional score-based diffusion models for Bayesian inference in infinite dimensions”. In: *Thirty-seventh Conference on Neural Information Processing Systems*. 2023.
- [5] Ricardo Baptista et al. *Memorization and Regularization in Generative Diffusion Models*. 2025. arXiv: 2501.15785 [cs.LG]. URL: <https://arxiv.org/abs/2501.15785>.
- [6] Hanene Ben Yedder et al. “Deep learning based image reconstruction for diffuse optical tomography”. In: *Machine Learning for Medical Image Reconstruction: First International Workshop, MLMIR 2018, Held in Conjunction with MICCAI 2018, Granada, Spain, September 16, 2018, Proceedings 1*. Springer. 2018, pp. 112–119.
- [7] C. E. Rasmussen and C. K. I. Williams. *Gaussian Processes for Machine Learning*. the MIT Press, Cambridge, MA, 2006.
- [8] Hyungjin Chung et al. “Diffusion Posterior Sampling for General Noisy Inverse Problems”. In: *The Eleventh International Conference on Learning Representations*. 2023.
- [9] G. Da Prato. *An Introduction to Infinite-Dimensional Analysis*. Universitext. Springer Berlin Heidelberg, 2006. ISBN: 9783540290216.
- [10] Bin Deng et al. “FDU-net: deep learning-based three-dimensional diffuse optical image reconstruction”. In: *IEEE transactions on medical imaging* 42.8 (2023), pp. 2439–2450.

- [11] Sreemanti Dey et al. “Score-based Diffusion Models for Photoacoustic Tomography Image Reconstruction”. In: *ICASSP 2024 - 2024 IEEE International Conference on Acoustics, Speech and Signal Processing (ICASSP)*. 2024, pp. 2470–2474.
- [12] Zehao Dou and Yang Song. “Diffusion Posterior Sampling for Linear Inverse Problem Solving: A Filtering Perspective”. In: *The Twelfth International Conference on Learning Representations*. 2024.
- [13] Lawrence C Evans. *Partial differential equations*. eng. Second edition. Graduate studies in mathematics. Providence, Rhode Island: American Mathematical Society, 2022. ISBN: 1470469421.
- [14] Berthy T. Feng et al. “Score-Based Diffusion Models as Principled Priors for Inverse Imaging”. In: *2023 IEEE/CVF International Conference on Computer Vision (ICCV)*. 2023, pp. 10486–10497.
- [15] Jonathan Ho, Ajay Jain, and Pieter Abbeel. “Denoising diffusion probabilistic models”. In: *Proceedings of the 34th International Conference on Neural Information Processing Systems*. NIPS ’20. Vancouver, BC, Canada: Curran Associates Inc., 2020. ISBN: 9781713829546.
- [16] Yoko Hoshi and Yukio Yamada. “Overview of diffuse optical tomography and its clinical applications”. In: *Journal of biomedical optics* 21.9 (2016), pp. 091312–091312.
- [17] Steven L Jacques. “Optical properties of biological tissues: a review”. In: *Physics in Medicine & Biology* 58.11 (2013), R37.
- [18] Jari Kaipio and Erkki Somersalo. *Statistical and computational inverse problems*. Vol. 160. Springer Science & Business Media, 2006.
- [19] Benjamin Lambert et al. “Trustworthy clinical AI solutions: a unified review of uncertainty quantification in deep learning models for medical image analysis”. In: *Artificial Intelligence in Medicine* (2024), p. 102830.
- [20] Zongyi Li et al. “Fourier Neural Operator for Parametric Partial Differential Equations”. In: *International Conference on Learning Representations*. 2021.
- [21] Jiulong Liu, Nanguang Chen, and Hui Ji. “Learnable Douglas-Rachford iteration and its applications in DOT imaging.” In: *Inverse Problems & Imaging* 14.4 (2020).
- [22] Ilya Loshchilov and Frank Hutter. “Decoupled Weight Decay Regularization”. In: *International Conference on Learning Representations*. 2019.

- [23] Meghdoot Mozumder, Jarkko Leskinen, and Tanja Tarvainen. “Utilising nanosecond sources in diffuse optical tomography”. In: *Measurement Science and Technology* 34.2 (Nov. 2022), p. 025901.
- [24] Meghdoot Mozumder et al. “A model-based iterative learning approach for diffuse optical tomography”. In: *IEEE Transactions on Medical Imaging* 41.5 (2021), pp. 1289–1299.
- [25] Adam Paszke et al. “PyTorch: An Imperative Style, High-Performance Deep Learning Library”. In: *Advances in Neural Information Processing Systems*. Ed. by H. Wallach et al. Vol. 32. Curran Associates, Inc., 2019.
- [26] Jakiw Pidstrigach et al. “Infinite-Dimensional Diffusion Models”. In: *Journal of Machine Learning Research* 25.414 (2024), pp. 1–52. URL: <http://jmlr.org/papers/v25/23-1271.html>.
- [27] Simo Särkkä and Arno Solin. *Applied Stochastic Differential Equations*. Institute of Mathematical Statistics Textbooks. Cambridge University Press, 2019.
- [28] Fabian Schneider et al. “An Unconditional Representation of the Conditional Score in Infinite Dimensional Linear Inverse Problems”. In: *Transactions on Machine Learning Research* (2025). ISSN: 2835-8856.
- [29] Martin Schweiger and Simon R. Arridge. “The Toast++ software suite for forward and inverse modeling in optical tomography”. In: *Journal of Biomedical Optics* 19.4 (2014), p. 040801.
- [30] Jascha Sohl-Dickstein et al. “Deep Unsupervised Learning using Nonequilibrium Thermodynamics”. In: *Proceedings of the 32nd International Conference on Machine Learning*. Ed. by Francis Bach and David Blei. Vol. 37. Proceedings of Machine Learning Research. Lille, France: PMLR, Sept. 2015, pp. 2256–2265.
- [31] Yang Song et al. “Score-Based Generative Modeling through Stochastic Differential Equations”. In: *International Conference on Learning Representations*. 2021.
- [32] Yang Song et al. “Solving Inverse Problems in Medical Imaging with Score-Based Generative Models”. In: *International Conference on Learning Representations*. 2022.
- [33] Andrew M Stuart. “Inverse problems: a Bayesian perspective”. In: *Acta numerica* 19 (2010), pp. 451–559.
- [34] T. Durduran et al. “Diffuse optics for tissue monitoring and tomography”. In: *Rep. Prog. Phys.* 73 (2015), p. 076701.

- [35] Pascal Vincent. “A Connection Between Score Matching and Denoising Autoencoders”. In: *Neural Computation* 23.7 (2011), pp. 1661–1674.
- [36] Wujun Xu et al. “Scalable Synthesis of Biodegradable Black Mesoporous Silicon Nanoparticles for Highly Efficient Photothermal Therapy”. In: *ACS Applied Materials & Interfaces* 10.28 (2018), pp. 23529–23538.
- [37] Huangjian Yi et al. “Enhanced model iteration algorithm with graph neural network for diffuse optical tomography”. In: *Biomedical Optics Express* 15.3 (2024), pp. 1910–1925.
- [38] Jaejun Yoo et al. “Deep learning diffuse optical tomography”. In: *IEEE transactions on medical imaging* 39.4 (2019), pp. 877–887.
- [39] Xinzhen Yu et al. “High-fidelity diffuse optical tomography imaging based on MRI physics information-constrained stacked autoencoder neural network”. In: *Optics Communications* 583 (2025), p. 131753.
- [40] Fangzhou Zhao et al. “Reproducibility of identical solid phantoms”. In: *Journal of Biomedical Optics* 27.7 (2022), p. 074713.
- [41] Yun Zou et al. “Machine learning model with physical constraints for diffuse optical tomography”. In: *Biomedical optics express* 12.9 (2021), pp. 5720–5735.